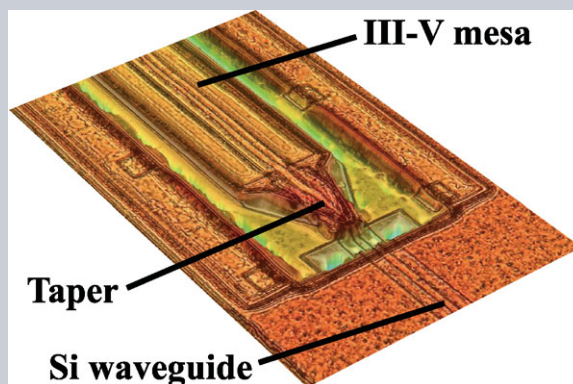


Abstract A semiconductor optical amplifier at 2.0- μm wavelength is reported. This device is heterogeneously integrated by directly bonding an InP-based active region to a silicon substrate. It is therefore compatible with low-cost and high-volume fabrication infrastructures, and can be efficiently coupled to other active and passive devices in a photonic integrated circuit. On-chip gain larger than 13 dB is demonstrated at 20 °C, with a 3-dB bandwidth of ~ 75 nm centered at 2.01 μm . No saturation of the gain is observed for an on-chip input power up to 0 dBm, and on-chip gain is observed for temperatures up to at least 50 °C. This technology paves the way to chip-level applications for optical communication, industrial or medical monitoring, and non-linear optics.



Semiconductor optical amplifiers at 2.0- μm wavelength on silicon

Nicolas Volet^{1,*}, Alexander Spott¹, Eric J. Stanton¹, Michael L. Davenport¹, Lin Chang¹, Jon D. Peters¹, Travis C. Briles², Igor Vurgaftman³, Jerry R. Meyer³, and John E. Bowers¹

1. Introduction

Interest in the spectral region around 2.0- μm wavelength includes the detection of molecules such as CO_2 and H_2O for industrial process control and environmental monitoring [1–3]. It is also valuable for non-invasive blood glucose measurements [4] and laser surgery [5]. Beside, it represents a promising eye-safe transmission window for optical communication with hollow-core photonic-bandgap fibers [6, 7] and for non-linear optics with microstructured chalcogenide fibers [8]. These applications have triggered the research and development of mid-infrared lasers with various specifications [9]. In particular, the recent demonstration of a 2.0- μm laser [10] and of a 2.35- μm photo-diode [11] heterogeneously integrated on a silicon (Si) substrate are important steps towards low-cost, high-volume, and compact photonic integrated circuits (PICs). They leverage the very mature complementary metal-oxide-semiconductor (CMOS) fabrication infrastructures [12, 13], which drive most electronic technologies. The simultaneous low two-photon absorption coefficient and high Kerr coefficient of Si around 2.0 μm [14] make it an attractive platform for future integration with broadband frequency combiners [15] and for power-efficient chip-level applications in non-linear optics [16–18]. These include in particular comb generation and frequency doubling [19, 20]. Beside their primary purpose of light amplification, semiconductor optical amplifiers (SOAs) are basic building blocks for ultra-fast all-optical signal processing

devices, such as spectral converters, dispersion compensators, and optical de-multiplexers [21]. When designed for 1.55- μm wavelength, they are commonly used in wavelength-division multiplexing (WDM) transmitters after the spectral combiner. SOAs heterogeneously integrated on Si have recently attracted considerable attention [13, 22–24], even though they were first demonstrated a decade ago [25]. Here we report, a SOA at 2.0- μm wavelength. This device is heterogeneously integrated on Si [26], and thus opens up new possibilities for advanced PICs.

2. SOA design and fabrication

The design of these 2.0- μm SOAs is based on our recently demonstrated 2.0- μm heterogeneously integrated Si lasers [10]. As illustrated in Fig. 1(a), a 0.50- μm thick partially etched Si rib waveguide is defined by deep-ultraviolet lithography on a Si-on-insulator (SOI) wafer with a 1- μm thick buried SiO_2 layer. The epitaxial layers of the active region, with four GaInAs quantum wells, are grown (by nLIGHT, Inc.) with metalorganic vapour phase epitaxy (MOVPE) on an InP substrate. These wells are compressively strained, thus favoring optical gain for TE-polarized light [27]. The InP and the SOI wafers are directly bonded by plasma-assisted wafer bonding and annealed at 300 °C for 60 min while pressed together with a graphite bonding fixture [28]. An InP/GaInPAs super-lattice is used to

¹ Department of Electrical and Computer Engineering, University of California, Santa Barbara (UCSB), CA 93106, USA

² National Institute of Standards and Technology (NIST), 325 Broadway, Boulder, CO 80305, USA

³ US Naval Research Laboratory, Washington, DC 20735, USA

*Corresponding author: e-mail: volet@ece.ucsb.edu

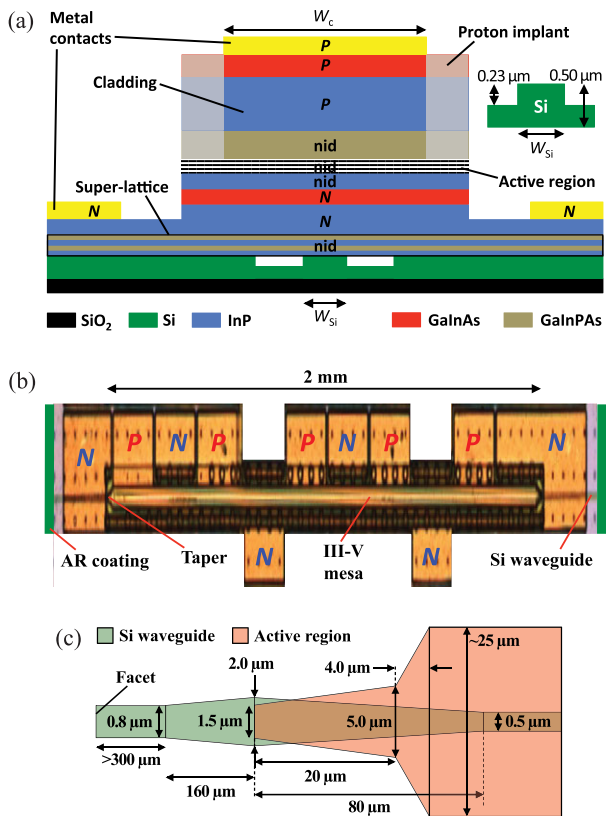


Figure 1 (a) Simplified cross-section schematic of the SOA, with the indication of the doping types. Inset shows the cross-section of the Si rib waveguide. (b) Top-view micrograph of the device. The image height is magnified 4 \times . The different *N*- and *P*-contacts are indicated. The 2-mm long III-V mesa terminates with tapers on both sides. Two thick green lines indicate the location of the AR coating layers. (c) Top-view schematic of the taper, in the horizontal plane of the active region.

prevent bonding dislocations from propagating to the active region [29, 30]. The InP substrate is removed by mechanical lapping followed by 3:1 HCl:H₂O wet etching. A ~ 25 - μm wide III-V mesa is formed by CH₄/H₂/Ar reactive ion etching (RIE) with a SiO₂ hard mask. This width value is a trade-off to minimize both the thermal impedance of the heat sink and the series resistance of the whole device [31]. As seen in Fig. 1(b)–(c), this mesa is terminated on both sides by a lateral taper of the active region to a ~ 1.5 - μm tip, causing the active hybrid mode to couple into a passive Si waveguide mode. The reflectance of the taper can be extracted by fitting ASE spectra of the device with a matrix-element method [31]. This procedure leads to an estimated value of -18 dB, which agrees well with simulations based on the finite-difference time-domain (FDTD) method. Under the III-V mesa, the width W_{Si} of the Si rib waveguide is 0.5 μm to maximize the transverse optical confinement factor Γ_{xy} in the active region [10, 31], whereas it is 0.8 μm at the facets. It is flared to 2.0 μm underneath the taper tip to reduce Γ_{xy} in the narrow taper.

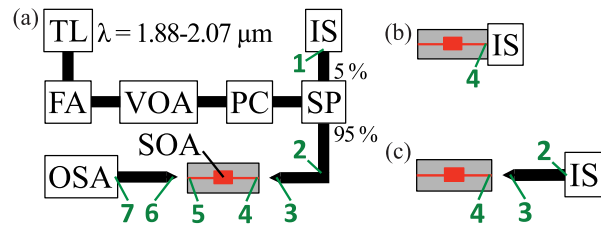


Figure 2 (a) Schematic of the experimental setup, including tunable laser (TL), fiber amplifier (FA), variable optical attenuator (VOA), polarization controller (PC), splitter (SP), integrating sphere (IS), and optical spectrum analyser (OSA). (b)–(c) Schematic of the measurement of the loss L_C from the amplified spontaneous emission measured with the IS (b) placed close to the SOA waveguide, and (c) connected to the lensed fiber.

Notice that having the Si waveguide at the facets allows the characterization of an SOA that can be used as a sub-component in a PIC. Bottom contacts (Pd/Ge/Pd/Au) and top contacts (Pd/Ti/Pd/Au) are deposited respectively on *N*-InP and on *P*-GaInAs. A current channel is then formed by proton implantation, with a width $W_c = 6$ μm . The *N*- and the *P*-contacts are electrically isolated from each other by sputtering 1 μm of SiO₂. The polished Si waveguide facets are antireflective (AR) coated with 1 pair of Ta₂O₅/SiO₂ layers having an estimated reflectance below -27 dB.

3. Experiments

The sample is mounted on a temperature-controlled Cu stage and current is delivered via a source measurement unit (Keithley) and micro-probes (Wentworth). Input light is provided by two continuous-wave, single-mode lasers widely tunable around 2- μm wavelength. The Thorlabs TLK-L1950R is used for 1.88–2.02 μm and the Newport Velocity TLB-6736 for 1.99–2.07 μm . A schematic of the setup is shown in Fig. 2(a). Incident laser light is coupled into single-mode fibers and intensified with a fiber amplifier (AdValue Photonics). A variable optical attenuator (OZ Optics) then adjusts the pump power and an in-line polarization controller (Thorlabs PLC-900) rotates the polarization so the TE-polarized mode is input to the SOA. The laser light is then split with a coupler (FONT Co.), so that $\sim 5\%$ of the pump is sent to an integrating sphere (IS) with a GaInAs photo-diode power sensor (Thorlabs S148C). Light is coupled in and out of the SOA by tapered lensed fibers (OZ Optics) attached to V-groove fiber holders (Thorlabs HFV002) placed on three-axis positioning stages (Newport 562F with piezo actuators PZA12). The light amplified by the SOA is then coupled to an optical spectrum analyzer (OSA, Yokogawa AQ6375) via the output lensed fiber.

The green labels $j = 1, \dots, 7$ in Fig. 2(a) indicate the locations of the corresponding powers P_j used to determine the on-chip gain factor. The power P_1 measured by the IS is used to monitor the power P_4 incident on the SOA. This is achieved by first calibrating the dependence of the

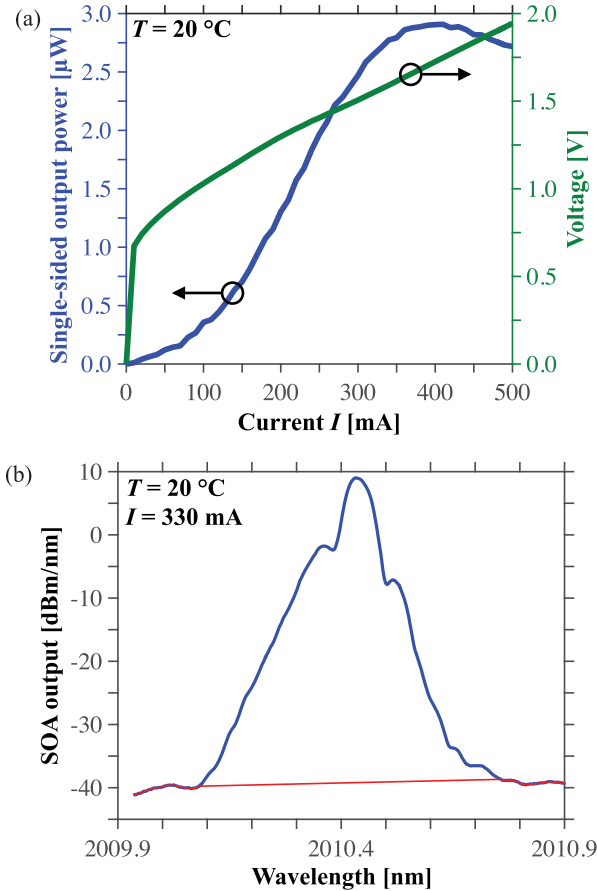


Figure 3 (a) Power-current characteristic (left, blue axis) of the SOA measured at 20 °C in the configuration of Fig. 2(c) and voltage-current characteristic (right, green axis). (b) SOA output spectrum measured with a $\sim 2.01\text{-}\mu\text{m}$ pump at 20 °C and 330 mA. The red curve indicates the ASE level involved in the computation of the noise figure.

splitting ratio $R_{\text{sp}} = P_2/P_1$ on the pump wavelength λ with the OSA, and by measuring the loss $L_c = P_4/P_2$ with the IS. This last step is schematized in Fig. 2(b)–(c). Notice that L_c includes the fiber attenuation P_3/P_2 and the coupling efficiency P_4/P_3 between the lensed fiber tip and the SOA waveguide. For both P_1 and P_7 , care is also taken to determine the fraction of pump power that is in the spectral range centered about λ and spanning 1 nm. This is to exclude the spontaneous emission from the computation of the gain factor. The power P_5 amplified by the SOA is found from the power P_7 measured by the OSA in the same spectral range around λ , and by including the loss $L'_c = P_7/P_5$ also measured with the IS. The on-chip gain factor G can finally be computed from:

$$G = P_5/P_4 = \frac{P_7/P_1}{(P_2/P_1)(P_4/P_2)(P_7/P_5)} = \frac{P_7/P_1}{R_{\text{sp}}L_cL'_c}. \quad (1)$$

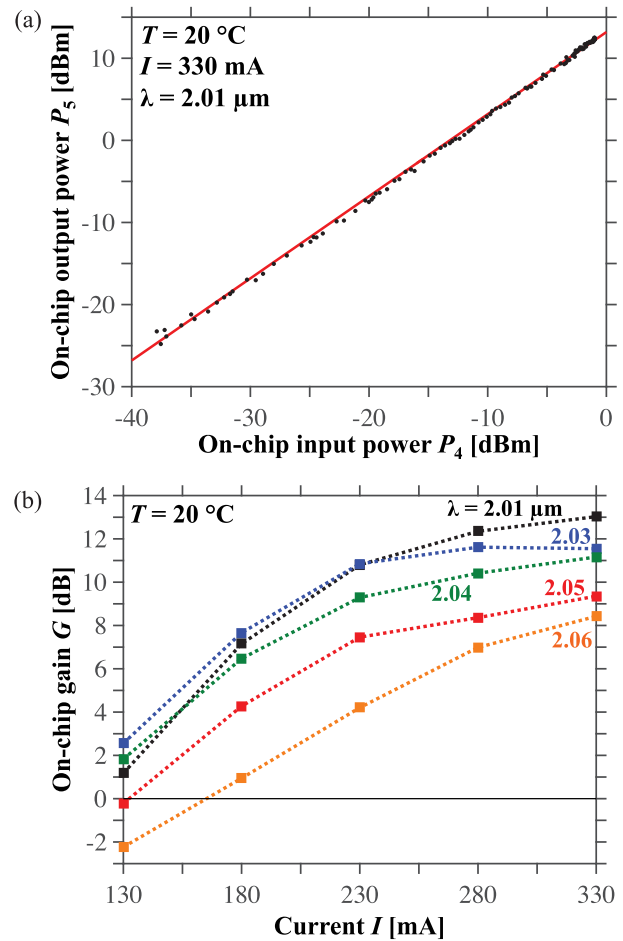


Figure 4 (a) On-chip output power P_5 measured at 20 °C and 330 mA as a function of the on-chip input power P_4 , for a 2.01- μm pump wavelength. The solid red line is a linear fit from which the on-chip gain factor is found using (1). (b) On-chip gain factor extracted at 20 °C as a function of the current, for different pump wavelengths λ . Dotted curves are guides for the eyes.

4. Results and discussion

Fig. 3(a) shows the power-current-voltage characteristics of the SOA, measured at 20 °C with no optical injection. Thermal roll-over is seen to occur for currents larger than ~ 300 mA. This device is then pumped as described in Fig. 2(a), with the commercial tunable lasers mentioned in Section 3. The SOA output spectrum, as illustrated in Fig. 3(b), is measured as a function of the incident power, at different temperatures, currents, and pump wavelengths. The on-chip output power can then be extracted. Figure 4(a) indicates that the relation between SOA input and output power is purely linear over the available range of on-chip input power (–40 dBm to 0 dBm). Therefore, no gain saturation is observed and relation (1) thus gives the on-chip gain factor in the unsaturated (or “small-signal”) regime.

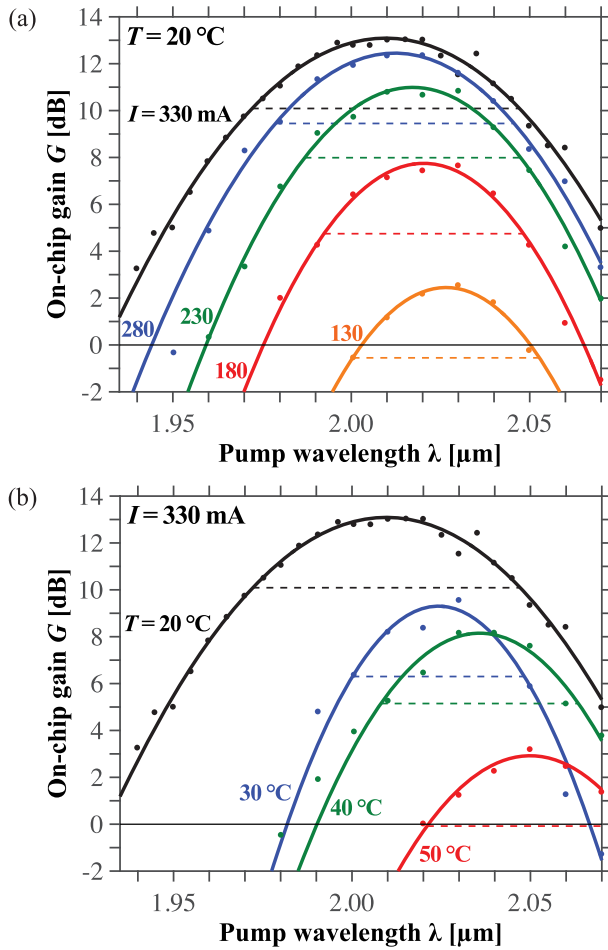


Figure 5 Spectral dependence of the on-chip gain factor measured (a) at 20 °C and different currents I , and (b) at 330 mA and different temperatures T . Solid curves are fits with (3) and dashed lines indicate the respective 3-dB bandwidths $\Delta\lambda_{1/2}$.

Gain factors extracted at 20 °C and different pump wavelengths λ are plotted in Fig. 4(b) as a function of the current. Depending on λ , on-chip gain is observed for currents larger than 130 mA. The largest value of $G \cong 13.1$ dB is measured at $\lambda = 2.01$ μm , $I = 330$ mA, and $V \cong 1.6$ V.

Due to thermal roll-over [see Fig. 3(a)], the gain factor is not expected to increase significantly for higher currents.

The input saturation power of the SOA can be estimated from [32]:

$$P_{\text{in,s}} \cong \frac{2 \ln(2) \, ch \, \sigma_{xy}}{G - 2 \, \Gamma_{xy} \, a \lambda \tau}, \quad (2)$$

where c is the speed of light in vacuum, h Planck's constant, $\sigma_{xy} \cong 0.17$ μm^2 the cross-section area of the active region, a the differential gain, and τ the recombination lifetime. Typical values for GaInAs quantum wells are $a \cong 10^{-15}$ cm^2 [33], and $\tau \cong 1$ ns [34]. Assuming a uniform carrier distribution only within the 6- μm wide current channel, numerical simulations give $\Gamma_{xy} \cong 4.7 \cdot 10^{-2}$. For $G = 13.1$ dB $\cong 20.4$, one thus finds an input saturation power $P_{\text{in,s}} \cong -5.9$ dBm. This value is smaller than the maximal available on-chip input power. Therefore, gain saturation is expected to occur, but it is not observed in the experimental data [see Fig. 4(a)]. The discrepancy is probably due to the approximations involved in the derivation of (2) and to the uncertainty in the values for a and τ . Notice from (2) that an inherent advantage of the present heterogeneously integrated platform is that the Si waveguide width can be modified to tune the gain and gain saturation through a variation of the transverse optical confinement factor Γ_{xy} .

Fig. 5(a) shows the on-chip gain factor G of the SOA extracted as a function of the pump wavelength λ at 20 °C and different currents. Its spectral variation at 330 mA is presented in Fig. 5(b) for different temperatures. On-chip gain is observed up to at least 50 °C.

At a fixed current and a fixed temperature, the spectral dependence of the on-chip gain factor can be described by [35]:

$$G(\lambda) = G_p \exp \left[-A (\lambda - \lambda_p)^2 \right], \quad (3)$$

where $G_p \equiv \exp[g_{\text{net}}(\lambda_p)L]$ is the peak value of G with g_{net} the net modal gain, $L = 2$ mm the length of the active region, and λ_p is the peak gain wavelength. The parameter A depends on L , on Γ_{xy} and on the material gain g . It is related to the 3-dB gain bandwidth of the SOA by $\Delta\lambda_{1/2} = 2\sqrt{\ln(2)/A}$. The experimental data of Fig. 5 are fitted with (3), showing excellent agreement (coefficients

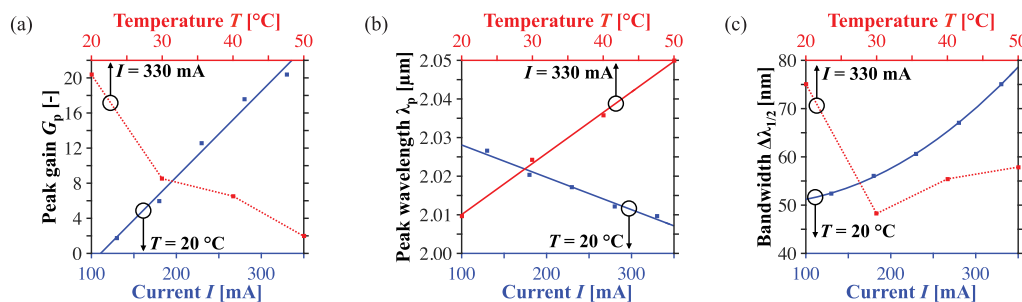


Figure 6 Fitted values extracted for (a) the peak gain G_p plotted in linear scale, (b) the peak gain wavelength λ_p and (c) the 3-dB gain bandwidth $\Delta\lambda_{1/2}$ of the SOA. Data are plotted at 20 °C as a function of the current (bottom, blue axis), and under 330 mA as a function of the temperature (top, red axis). Solid curves are either linear or quadratic fits and dotted curves are guides for the eyes.

of determination $R^2 > 0.99$). The extracted values for G_p , λ_p , and $\Delta\lambda_{1/2}$ are presented in Fig. 6.

It is found in Fig. 6(a) that the peak value of the gain factor increases linearly with the current, with:

$$\frac{\partial G_p}{\partial I} = G_p \Gamma_{xy} L \frac{\partial g_p}{\partial I} \cong 9.77 \cdot 10^{-2} \text{ mA}^{-1}. \quad (4)$$

This linear behavior can be accounted for by approximating the peak value g_p of the material gain with the following logarithmic relation [36]:

$$\Gamma_{xy} g_p L \cong \ln \left(\frac{I + I_s}{I_{tr} + I_s} \right), \quad (5)$$

where $I_{tr} \cong 121 \text{ mA}$ is the current at transparency and the parameter I_s is related to the differential gain.

From Fig. 6(b), it is observed that as the current increases, the peak gain wavelength decreases linearly, with $\partial\lambda_p/\partial I \cong -83.8 \text{ pm}\cdot\text{mA}^{-1}$ (or equivalently $\partial f_p/\partial I \cong 6.17 \text{ GHz}\cdot\text{mA}^{-1}$, where f_p is the peak gain frequency). This can be explained with the combination of Burstein's band filling effect [37] and the free-carrier plasma loading [38], both arising from the increase of carrier density with the current. The resultant effect dominates over the thermo-optic effect [39,40] and thermal expansion caused by Joule heating. Therefore, as the current increases, the effective refractive index decreases and so does the peak gain wavelength. In contrast, as the temperature of the stage is increased for a fixed current, the thermo-optic effect is dominant. In this case, as seen in Fig. 6(b), λ_p increases linearly with the temperature, with $\partial\lambda_p/\partial T \cong 1.32 \text{ nm}\cdot\text{K}^{-1}$.

The data of Fig. 6(c) suggest that the 3-dB gain bandwidth $\Delta\lambda_{1/2}$ of the SOA at 20°C depends quadratically on the current. This can be understood from the spectral broadening of the material gain with the carrier density [41,42]. In particular, a maximum value of $\Delta\lambda_{1/2} \cong 75 \text{ nm}$ is obtained at 20°C and 330 mA .

Coupling between the amplitude and phase of the electric field in a semiconductor cavity can be characterized with the linewidth enhancement factor [43]. This figure-of-merit is defined from the carrier-induced change of real and imaginary parts of the refractive index, and can be expressed as [44,45]:

$$\alpha_H = \frac{4\pi}{c} n_g \frac{\partial f_p}{\partial I} \left(\frac{\partial g_p}{\partial I} \right)^{-1}. \quad (6)$$

The effective group index $n_g \cong 3.8$ is found in the present case from the ripples caused on the ASE spectrum by internal reflections in the SOA waveguide. Using (4), the previous expression can be rewritten and computed as:

$$\alpha_H = \frac{4\pi}{c} n_g \Gamma_{xy} L \frac{\partial f_p}{\partial I} \left(\frac{\partial G_p}{\partial I} \right)^{-1} G_p \cong 0.94 G_p. \quad (7)$$

It was discussed at Fig. 6(a), that the peak value G_p of the on-chip gain factor increases linearly with current. Expression (7) indicates that this linearity also holds for the

linewidth enhancement factor. This result is in agreement with previous reports [46,47] where α_H was extracted in SOAs by different methods. Notice that using an SOA to extract the linewidth enhancement factor of an active region has the advantage of not being limited to currents below lasing threshold. At 20°C and 330 mA , where $G_p \cong 20.4$, relation (7) allows to estimate $\alpha_H \cong 19.3$. Lower values of α_H are desirable in semiconductor lasers, where this parameter increases the laser linewidth and is responsible for the unwanted spectral chirping when the devices are modulated [48]. This is also the case for SOAs used in transmission systems, in order to reduce the chirp undergone by a large pulse going through the device. However, when used for cross-phase modulation (XPM), SOAs must produce a large phase shift with minimal intensity variation. [21,49]. Therefore, in this particular case of wavelength converters, large values of α_H are preferred. Notice that the present design can be readily modified to tune α_H by changing the confinement, either with the Si waveguide width, or with the device length.

The noise figure F characterizes the deterioration of the signal-to-noise ratio as the amplified light propagates through the SOA [50]. It is a crucial parameter for practical use of the SOA. The main contributions are the shot noise $F_{\text{shot}} = 1/G$ due to the amplified signal, and the excess noise $F_{\text{sig-ASE}}$ caused by the beating between the signal and the ASE [51]. This last term is given by [52]:

$$F_{\text{sig-ASE}} = \frac{2}{G} \frac{\lambda^3}{c^2 h} \frac{P_{\text{ASE},\parallel}}{\delta\lambda}, \quad (8)$$

where $P_{\text{ASE},\parallel}$ is the forward propagating ASE power measured in the wavelength range $\delta\lambda$ around λ and co-polarized with the signal. In the present case where the SOA gain is strongly favored for TE-polarized light, $P_{\text{ASE},\parallel} \cong P_{\text{ASE}}$. From Fig. 3(b), $P_{\text{ASE}}/\delta\lambda \cong -24.3 \text{ dBm}\cdot\text{nm}^{-1}$ at 20°C and 330 mA , and a moderate noise figure $F \cong 17.2 \text{ dB}$ is found at the peak gain wavelength of $2.01 \mu\text{m}$. Lower values of F are expected if the SOA is pumped with higher input powers. Indeed, due to the reduction of the spontaneous emission factor and the relatively low contribution of the shot noise, the noise figure reaches a minimum as the gain is saturated [50].

5. Conclusions and outlook

We have demonstrated a 2.0- μm wavelength SOA heterogeneously integrated on silicon. On-chip gain larger than 13 dB is reported at 20°C , with a 3-dB bandwidth of 75 nm. This SOA operates up to at least 50°C and is heterogeneously integrated on silicon. It can thus be efficiently coupled to other active and passive devices fabricated with the CMOS infrastructures. We believe that this is a key technology for numerous chip-level applications in this spectral range, including spectroscopy, communication, and non-linear optics.

Acknowledgements. This work is supported by a DARPA MTO DODOS contract (HR0011-15-C-055) and the U.S. Office of Naval Research (ONR) under grant number N00014-13-C-0147. N.V. acknowledges support from the Swiss National Science Foundation. We thank Craig Goldberg from Newport for loaning the Velocity TLB-6736 tunable laser, and Alexander Wilson from Keyence for performing high-resolution micrographs of the samples. We also thank Alan Y. Liu and Christos T. Santis for valuable discussions, along with Scott B. Papp and Scott A. Diddams for experimental assistance.

Received: 16 June 2016, **Revised:** 27 November 2016,

Accepted: 11 January 2017

Published online: 1 March 2017

Key words: Semiconductor optical amplifiers, silicon photonics, heterogeneous integration, mid-infrared.

References

- [1] R. J. De Young and N. P. Barnes, *Appl. Opt.* **49**, 562–567 (2010).
- [2] S. Ishii, K. Mizutani, H. Fukuoka, T. Ishikawa, B. Philippe, H. Iwai, T. Aoki, T. Itabe, A. Sato, and K. Asai, *Appl. Opt.* **49**, 1809–1817 (2010).
- [3] A. Khan, D. Schaefer, L. Tao, D. J. Miller, K. Sun, M. A. Zondlo, W. A. Harrison, B. Roscoe, and D. J. Lary, *Remote Sens.* **4**, 1355–1368 (2012).
- [4] N. V. Alexeeva and M. A. Arnold, *J. Diabetes Sci. Technol.* **3**, 219–232 (2009).
- [5] B. Chen, S. L. Thomsen, R. J. Thomas, J. Oliver, and A. J. Welch, *Lasers Surg. Med.* **40**, 358–370 (2008).
- [6] P. J. Roberts, F. Couny, H. Sabert, B. J. Mangan, D. P. Williams, L. Farr, M. W. Mason, A. Tomlinson, T. A. Birks, J. C. Knight, and P. S. J. Russell, *Opt. Express* **13**, 236–244 (2005).
- [7] Y. Chen, Z. Liu, S. R. Sandoghchi, G. T. Jasion, T. D. Bradley, E. Numkam Fokoua, J. R. Hayes, N. V. Wheeler, D. R. Gray, B. J. Mangan, R. Slavík, F. Poletti, M. N. Petrovich, and D. J. Richardson, *J. Lightw. Technol.* **34**, 104–113 (2016).
- [8] S. Xing, D. Grassani, S. Kharitonov, A. Billat, and C. S. Brès, *Opt. Express* **24**, 9741–9750 (2016).
- [9] K. Scholle, S. Lamrini, P. Koopmann, and P. Fuhrberg, in: *Frontiers in Guided Wave Optics and Optoelectronics*, edited by B. Pal (InTech, 2010), chap. 21, pp. 471–500.
- [10] A. Spott, M. Davenport, J. Peters, J. Bovington, M. J. R. Heck, E. J. Stanton, I. Vurgaftman, J. Meyer, and J. Bowers, *Opt. Lett.* **40**, 1480–1483 (2015).
- [11] R. Wang, S. Sprengel, M. Muneeb, G. Boehm, R. Baets, M. C. Amann, and G. Roelkens, *Opt. Express* **23**, 26834–26841 (2015).
- [12] M. J. R. Heck, J. F. Bauters, M. L. Davenport, J. K. Doylend, S. Jain, G. Kurczveil, S. Srinivasan, Y. Tang, and J. E. Bowers, *IEEE J. Sel. Top. Quantum Electron.* **19**, 6100117 (2013).
- [13] G. Roelkens, A. Abassi, P. Cardile, U. Dave, A. de Groote, Y. de Koninck, S. Dhoore, X. Fu, A. Gassenq, N. Hattasan, Q. Huang, S. Kumari, S. Keyvaninia, B. Kuyken, L. Li, P. Mechet, M. Muneeb, D. Sanchez, H. Shao, T. Spuesens, A. Z. Subramanian, S. Uvin, M. Tassaert, K. van Gasse, J. Verbist, R. Wang, Z. Wang, J. Zhang, J. van Campenhout, X. Yin, J. Bauwelinck, G. Morthier, R. Baets, and D. van Thourhout, *Photonics* **3**, 969–1004 (2015).
- [14] A. D. Bristow, N. Rotenberg, and H. M. van Driel, *Appl. Phys. Lett.* **90**, 191104 (2007).
- [15] E. J. Stanton, M. J. R. Heck, J. Bovington, A. Spott, and J. E. Bowers, *Opt. Express* **23**, 11272–11283 (2015).
- [16] M. A. Foster, A. C. Turner, J. E. Sharping, B. S. Schmidt, M. Lipson, and A. L. Gaeta, *Nature* **441**, 960–963 (2006).
- [17] S. Zlatanovic, J. S. Park, S. Moro, J. M. Chavez Boggio, I. B. Divliansky, N. Alic, S. Mookherjea, and S. Radic, *Nature Photon.* **4**, 561–564 (2010).
- [18] P. Del’Haye, T. Herr, E. Gavartin, M. L. Gorodetsky, R. Holzwarth, and T. J. Kippenberg, *Phys. Rev. Lett.* **107**, 063901 (2011).
- [19] V. Brasch, E. Lucas, J. D. Jost, M. Geiselmann, and T. J. Kippenberg, *arXiv:1605.02801* (2016).
- [20] L. Chang, Y. Li, N. Volet, L. Wang, J. Peters, and J. E. Bowers, *Optica* **3**, 531–535 (2016).
- [21] K. E. Stubkjaer, *IEEE J. Sel. Top. Quantum Electron.* **6**, 1428–1435 (2000).
- [22] S. Keyvaninia, G. Roelkens, D. Van Thourhout, G. H. Duan, M. Lamponi, F. Lelarge, J. M. Fedeli, S. Messaoudene, E. J. Geluk, and B. Smalbrugge, in: *IEEE 9th International Conference on Group IV Photonics*, (2012), pp. 222–224.
- [23] S. Cheung, Y. Kawakita, K. Shang, and S. J. Ben Yoo, *Opt. Express* **23**, 22431–22443 (2015).
- [24] P. Kaspar, G. de Valicourt, R. Brenot, M. A. Mestre, P. Jennevé, A. Accard, D. Make, F. Lelarge, G. H. Duan, N. Pavarelli, M. Rensing, C. Eason, P. O’Brien, S. Olivier, S. Malhouitre, C. Kopp, C. Jany, and S. Menezes, *IEEE Photon. Technol. Lett.* **27**, 2383–2386 (2015).
- [25] H. Park, A. W. Fang, O. Cohen, R. Jones, M. J. Paniccia, and J. E. Bowers, *IEEE Photon. Technol. Lett.* **19**, 230–232 (2007).
- [26] N. Volet, A. Spott, E. J. Stanton, M. L. Davenport, J. D. Peters, J. R. Meyer, and J. E. Bowers, in: *Conference on Lasers and Electro-Optics*, (Optical Society of America, 2016), paper SM4G.4.
- [27] P. Koonath, S. Kim, W. J. Cho, and A. Gopinath, *IEEE J. Quantum Electron.* **38**, 1282–1290 (2002).
- [28] D. Liang, G. Roelkens, R. Baets, and J. E. Bowers, *Materials* **3**, 1782–1802 (2010).
- [29] L. Esaki and R. Tsu, *IBM J. Res. Develop.* **14**, 61–65 (1970).
- [30] A. Karim, K. A. Black, P. Abraham, D. Lofgreen, Y. J. Chiu, J. Piprek, and J. E. Bowers, *IEEE Photon. Technol. Lett.* **12**, 1438–1440 (2000).
- [31] M. L. Davenport, S. Skendžić, N. Volet, J. C. Hulme, M. J. R. Heck, and J. E. Bowers, *IEEE J. Sel. Top. Quantum Electron.* **22**, 3100111 (2016).
- [32] G. Bendelli, K. Komori, and S. Arai, *IEEE J. Quantum Electron.* **28**, 447–458 (1992).
- [33] S. D. Offsey, W. J. Schaff, L. F. Lester, L. F. Eastman, and S. K. McKernan, *IEEE J. Quantum Electron.* **27**, 1455–1462 (1991).
- [34] C. H. Henry, R. A. Logan, F. R. Merritt, and C. G. Bethea, *Electron. Lett.* **20**, 358–359 (1984).
- [35] M. Asada and Y. Suematsu, *IEEE J. Quantum Electron.* **21**, 434–442 (1985).

- [36] P. W. A. Mc Ilroy, A. Kurobe, and Y. Uematsu, *IEEE J. Quantum Electron.* **21**, 1958–1963 (1985).
- [37] G. W. Charache, D. M. DePoy, J. E. Reynolds, P. F. Bal-dasaro, K. E. Miyano, T. Holden, F. H. Pollak, P. R. Sharps, M. L. Timmons, C. B. Geller, W. Mannstadt, R. Asahi, A. J. Freeman, and W. Wolf, *J. Appl. Phys.* **86**, 452–458 (1999).
- [38] P. R. Selway, G. H. B. Thompson, G. D. Henshall, and J. E. A. Whiteaway, *Electron. Lett.* **10**, 453–455 (1974).
- [39] N. J. Dovichi and J. M. Harris, *Anal. Chem.* **51**, 728–731 (1979).
- [40] J. A. McCaulley, V. M. Donnelly, M. Vernon, and I. Taha, *Phys. Rev. B* **49**, 7408–7417 (1994).
- [41] G. Bastard, in: *Wave mechanics applied to semiconductor heterostructures* (Les Editions de Physique, 1988), pp. 272–302.
- [42] A. I. Kucharska and D. J. Robbins, *IEEE J. Quantum Elec-tron.* **26**, 443–448 (1990).
- [43] C. H. Henry, *IEEE J. Quantum Electron.* **18**, 259–264 (1982).
- [44] S. E. H. Turley, G. H. B. Thompson, and D. F. Lovelace, *Electron. Lett.* **15**, 256–257 (1979).
- [45] L. D. Westbrook, *Electron. Lett.* **21**, 1018–1019 (1985).
- [46] N. Storkfelt, B. Mikkelsen, D. S. Olesen, M. Yamaguchi, and K. E. Stubkjaer, *IEEE Photon. Technol. Lett.* **3**, 632–634 (1991).
- [47] S. Fu, W. Du, P. Shum, C. Wu, and L. Zhang, *IEEE Photon. Technol. Lett.* **18**, 1934–1936 (2006).
- [48] T. L. Koch and J. E. Bowers, *Electron. Lett.* **20**, 1038–1040 (1984).
- [49] L. Schares, C. Schubert, C. Schmidt, H. G. Weber, L. Occhi, and G. Guekos, *IEEE J. Quantum Electron.* **39**, 1394–1408 (2003).
- [50] E. Desurvire, *Appl. Opt.* **29**, 3118–3125 (1990).
- [51] D. M. Baney, P. Gallion, and R. S. Tucker, *Opt. Fib. Tech.* **6**, 122–154 (2000).
- [52] B. Pedersen, A. Bjarklev, J. H. Povlsen, K. Dybdal, and C. C. Larsen, *J. Lightw. Technol.* **9**, 1105–1112 (1991).